inorganics

MDPI

Article

Influence of Doping-Ion-Type on the Characteristics of Al_2O_3-Based Nanocomposites and Their Capabilities of Removing Indigo Carmine from Water

Fatima A. Adam

Chemistry Department, Faculty of Science, Imam Mohammad Ibn Saud Islamic University (IMSIU), P.O. Box 90905, Riyadh 11623, Saudi Arabia; famohamedali@imamu.edu.sa or leno.ali20789@gmail.com

Abstract: Globally, the continuous contamination of natural water resources is a severe issue, and looking for a solution for such a massive problem should be the researcher's concern. Herein, Al_2O_3, Al_2O_3-CuO, Al_2O_3-NiO, and Al_2O_3-CoO were prepared via a simple and fast route, utilizing glucose as a capping material. All synthesis conditions were uniform to make the fabricated nanomaterials' characteristics exclusively influenced by only the ion type. The SEM analysis showed that the particles of the synthesized Al_2O_3, Al_2O_3-CuO, Al_2O_3-NiO, and Al_2O_3-CoO were all less than 25 nm. The Al_2O_3-NiO showed the smallest particle size (11 to 14 nm) and the best BET surface area of 125.6 $m^2\ g^{-1}$. All sorbents were tested for removing organic pollutants, as exemplified by indigo carmine (IGC) dye. The Al_2O_3-NiO possessed the highest adsorption capacity among the other sorbents for which it had been selected for further investigations. The IGC sorption reached equilibrium within 2.0 h, and the kinetic study revealed that the IGC removal by Al_2O_3-NiO nanocomposite fitted the FOM and the LFM. The sorbent showed an experimental adsorption capacity (q_t) of 456.3 mg g^{-1} from a 200 mg L^{-1} IGC solution and followed the Langmuir model. The thermodynamic findings indicated an endothermic, spontaneous, and physisorption nature. The seawater and groundwater samples contaminated with 5.0 mg L^{-1} IGC concentrations were fully remediated using the Al_2O_3-NiO nanocomposite. The reuse study showed 93.3% average efficiency during four successive cycles. Consequently, prepared Al_2O_3-NiO nanocomposite is recommended for the treatment of contaminated water.

Keywords: aluminum oxide; nickel oxide; nanocomposite; adsorption; water treatment; indigo carmine

check for updates

Citation: Adam, F.A. Influence of Doping-Ion-Type on the Characteristics of Al_2O_3-Based Nanocomposites and Their Capabilities of Removing Indigo Carmine from Water. *Inorganics* **2022**, *10*, 144. https://doi.org/10.3390/inorganics10090144

Received: 20 August 2022
Accepted: 16 September 2022
Published: 19 September 2022

1. Introduction

Water pollution is among the most severe global problems threatening human health [1]. This prominent issue is a consequence of the rapid industrialization trend and continuous industrial waste discharge into water resources [2–5]. The pollutants in industrial effluents encompass organic dyes, pharmaceutical compounds, and heavy metals that pose authentic life problems [6]. Organic dyes with azo-groups, aromatic rings, or sulphonate groups are used extensively in various industries. Indigo carmine (Disodium [2(2)E]-3,3-dioxo-1,1,3,3-tetrahydro[2,2-biindolylidene]-5,5-disulfonate, IGC) is a highly water-soluble dye known to be toxic and carcinogenic [7,8]. Flocculation, chemical oxidation, ion exchange, and membranes have been used to remove such pollutants from water [9–17]. Unfortunately, these approaches were hindered by significant obstacles, such as low removal efficiency and/or high- cost [18–20]. The failure of conventional methods to eliminate organic pollutants is evident by detecting them in the tap water of many countries [21]. On the other hand, the adsorption and photodegradation processes perform better in removing such pollutants [22–26]. Although photocatalytic degradation requires no further treatment steps, it has been criticized for utilizing more energy and producing toxic fragments. Conversely, several sorbents show excellent efficiencies in eliminating organic pollutants, with the advantages of low energy consumption and without the formation of toxic products [27–30].

Seeking better sorbents with novel features, the researchers investigated synthesizing nanocomposites via doping by polymers, ceramics, and metal oxides. The suitability of doping materials significantly influences the molecular structure since they affect the aggregation of produced nanomaterial [31]. Traditionally, aluminum oxide (Al_2O_3) was known as an adsorbent in chromatography and a perfect bed-stabilizer for metal oxide catalysts. Al_2O_3 is an inexpensive, water-insoluble, rugged sorbent with a high surface area, and its surface encompasses both acidic and basic functional groups [32]. Hence, researchers are still interested in synthesizing Al_2O_3 in its pure and composite forms. Various studies have investigated the doping of Al_2O_3 by different amounts of the same element [33–38]. Nevertheless, the physical characteristics, adsorption capacity, and photocatalytic activity of the products can be affected by fabrication conditions, making it irrational to compare the ion-type impact.

This work aimed to prepare nanoscale Al_2O_3 and its CuO, NiO, and CoO nanocomposites via one fast, simple route. The synthesis conditions, doping amount, and calcination temperature will be uniform in order to eliminate any effects other than the ion type on the product's properties. The properties of the prepared nanomaterials will be investigated. Additionally, the better sorbent among the Al_2O_3, Al_2O_3-CuO, Al_2O_3-NiO, and Al_2O_3-CoO will be selected by studying the removal of IGC.

2. Results and Discussion

2.1. Characterization

Figure 1 illustrates the SEM results for the pure Al_2O_3, Al_2O_3-CuO, Al_2O_3-NiO, and Al_2O_3-CoO nanocomposites. The products showed cloudy-like clusters composed of tiny nanoparticles with size ranges of 18–22, 13–15, 11–14, and 14–20 nm for Al_2O_3, Al_2O_3-CuO, Al_2O_3-NiO, and Al_2O_3-CoO, respectively. The Al_2O_3-NiO nanoparticles being the smallest can be attributed to the strong NiO interaction with Al_2O_3, which facilitates NiO dispersion [39]. Furthermore, the elemental compositions of the fabricated nanomaterials were examined with EDX (Figure 2). The aluminum and oxygen mass percentages in the prepared Al_2O_3 nanoparticles were 52.7% and 47.3%, respectively; these results are almost typical of the theoretical Al_2O_3 composition. In their nanocomposites, Cu, Ni, and Co mass percentages were 8.7%, 5.1%, and 9.3%, respectively. Additionally, EDX mapping was employed to investigate the elemental distribution of the fabricated Al_2O_3, Al_2O_3-CuO, Al_2O_3-NiO, and Al_2O_3-CoO (Figure 3). The obtained maps of the doping ion followed the Al_2O_3 contours indicating an excellent dispersion of the Al_2O_3-metal-oxides phases without metal oxide accumulations.

XRD analysis was employed to investigate the crystallography of the prepared nanomaterials (Figure 4). Al_2O_3, Al_2O_3-CuO, Al_2O_3-NiO, and Al_2O_3-CoO results indicated amorphous confirmations that matched the SEM results. The diffraction peaks at $2\theta^{-}$ degrees of 37.3, 44.9, and 67.2 in all spectra were allocated to the Al_2O_3 phase (JCPDS card No. 37-1462) [32,40,41]. Although there is an overlap in the doping metal oxides and alumina results, the diffraction peaks at $2\theta^{\circ}$ of 62.72, 61.76, and 65.02 can be assigned to the CuO, NiO, and CoO phases in the nanocomposites [42–44].

Figure 5 illustrates the FTIR spectra for the Al_2O_3, Al_2O_3-CuO, Al_2O_3-NiO, and Al_2O_3-CoO. The most intense peaks around 740 and 908 cm^{-1} can be assigned to symmetric—asymmetric Al-O-Al stretching vibrations. The band at 560 cm^{-1} can be attributed to Al-O-Al bending and/or Cu-O stretching vibrations; Al-O also exhibited a band at 1150 cm^{-1} [42,45,46]. Additionally, peaks at 456 and 457 cm^{-1} in the Al_2O_3-NiO and Al_2O_3-CoO composites can be assigned to Ni-O and Co-O vibrations [44,47].

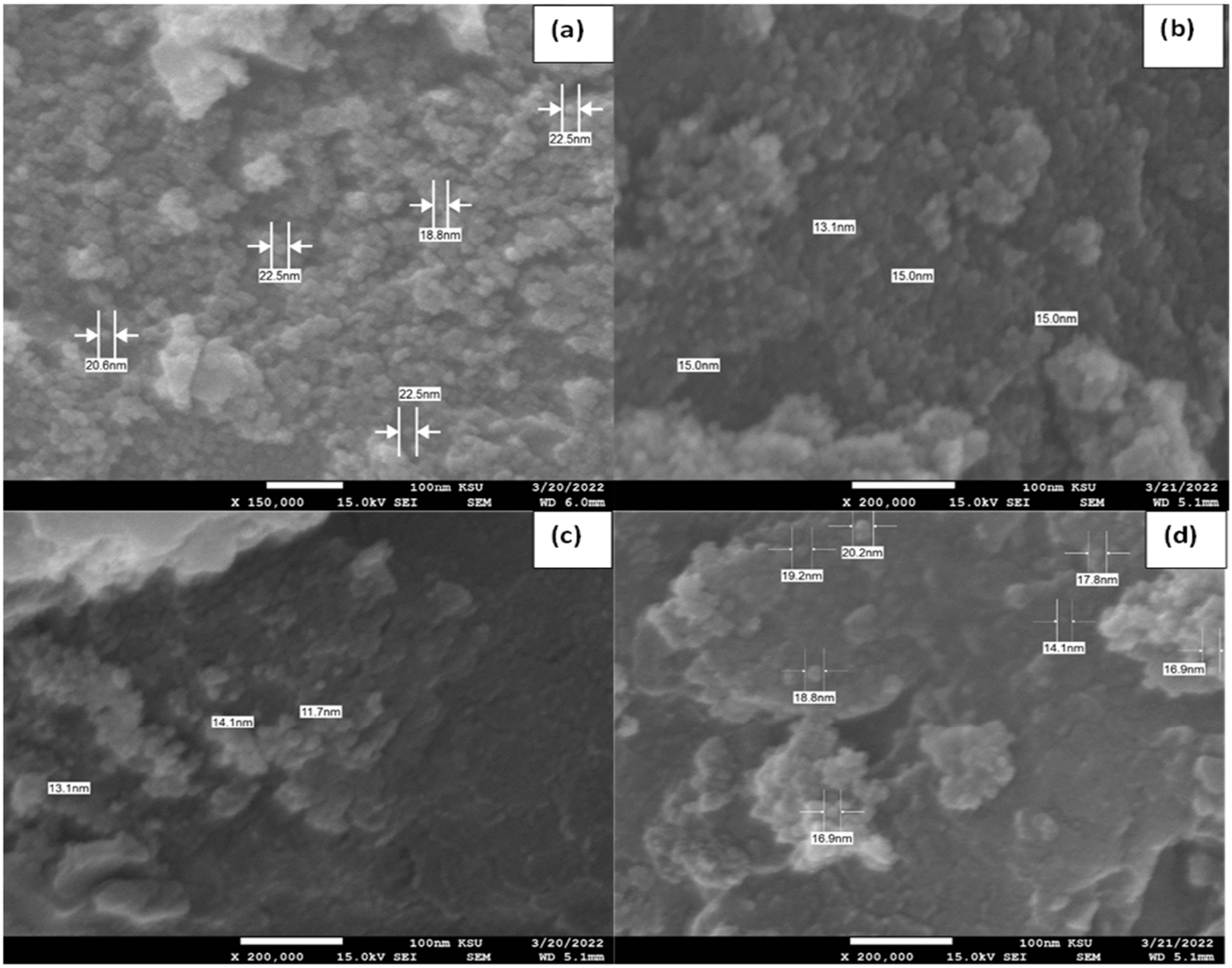

Figure 1. SEM results of the prepared (**a**) Al_2O_3 nanoparticles; (**b**–**d**) Al_2O_3 doped by CuO NiO, and CoO, respectively.

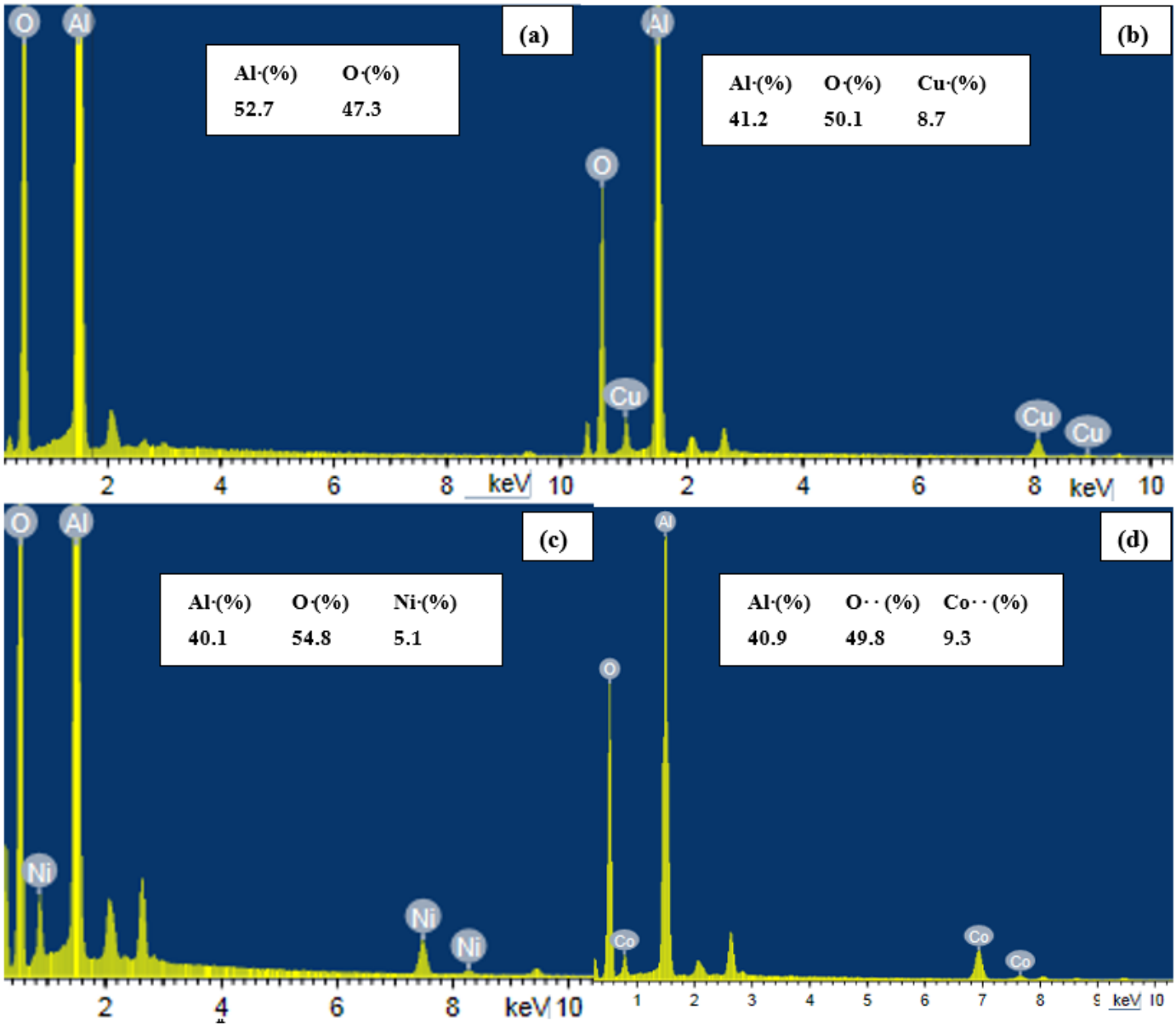

Figure 2. EDX results of the prepared (**a**) Al_2O_3 nanoparticles, (**b**–**d**) Al_2O_3 doped by CuO, NiO, and CoO, respectively.

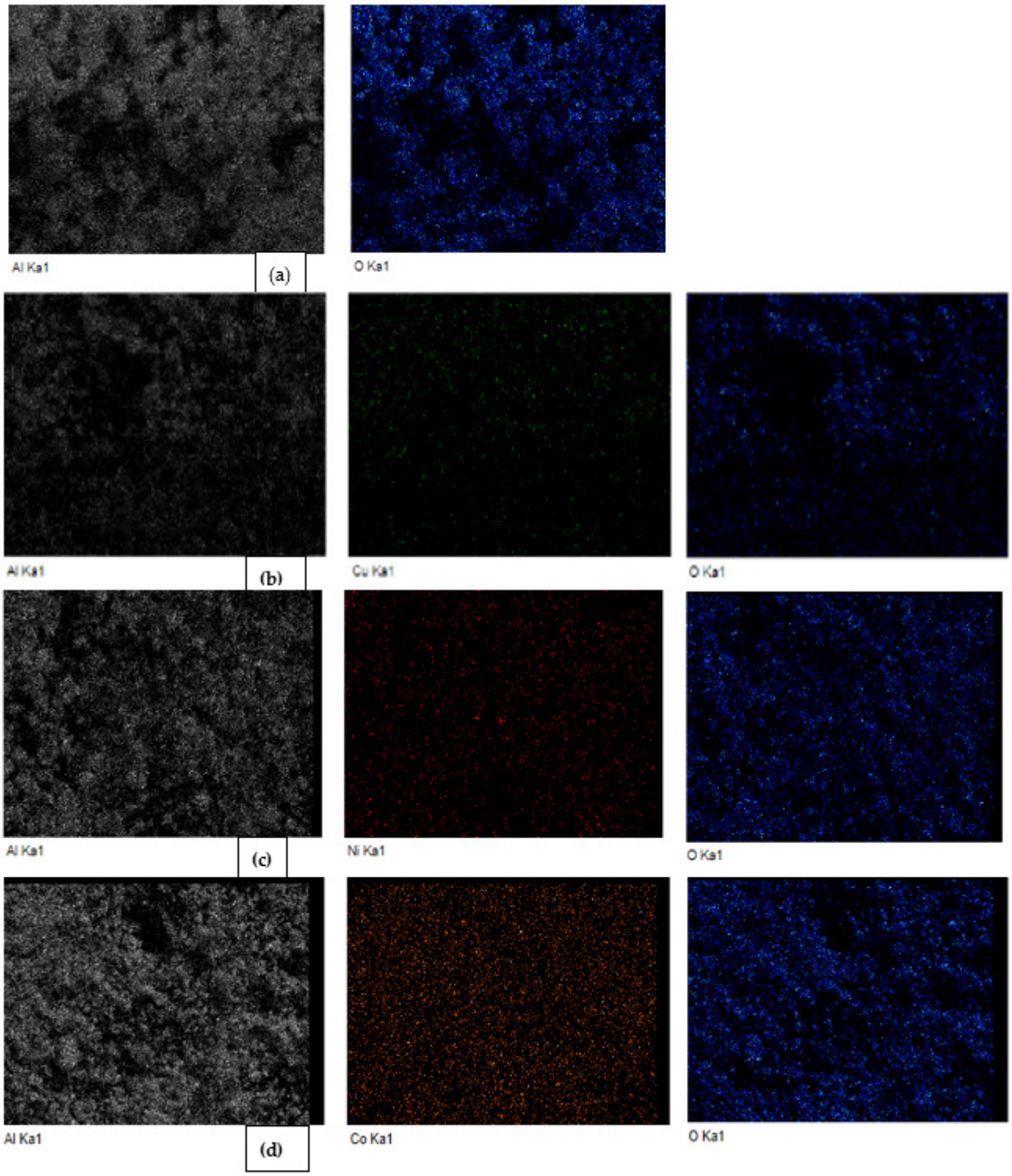

Figure 3. EDX mapping for the (**a**) Al_2O_3 nanoparticles, (**b**) Al_2O_3—CuO, (**c**) Al_2O_3—NiO, and (**d**) Al_2O_3—CoO nanocomposites.

Figure 4. The XRD results for (**a**) Al_2O_3 nanoparticle, (**b**) Al_2O_3—CuO, (**c**) Al_2O_3—NiO, and (**d**) Al_2O_3—CoO nanocomposites.

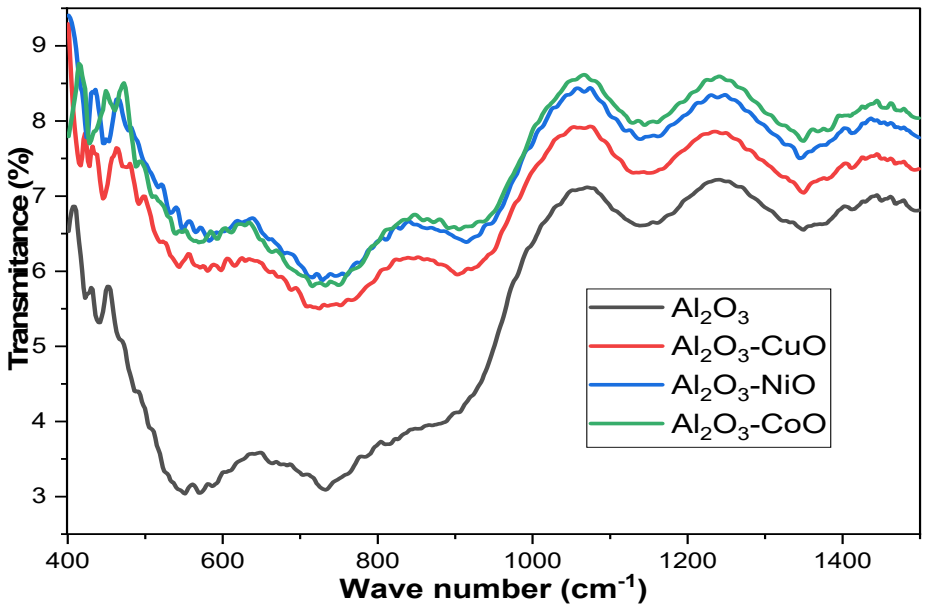

Figure 5. FTIR findings for the Al_2O_3 nanoparticle and its CuO, NiO, and CoO nanocomposites.

The N_2 adsorption-desorption-isotherm was employed to investigate the surface and porosity features of the Al_2O_3, Al_2O_3-CuO, Al_2O_3-NiO, and Al_2O_3-CoO (Figure 6). The pore diameter (PD) and pore volume (PV) were determined via the Barrett–Joyner–Halenda (BJH) method, while the BET method was utilized for determining the surface area (SA), and the results are gathered in Table 1. The Al_2O_3 nanoparticles and their CoO nanocomposites showed loop-hysteresis-type H3 allocated to slit-like non-rigid-aggregate particles with cylindrical micro-pores. Conversely, the Al_2O_3-CuO and Al_2O_3-NiO possessed loop-hysteresis-type H4 assigned to fluffy particles with slit-like micro-pores [48,49]. Al_2O_3-NiO nanocomposite exhibited the highest BET-SA, which follows the SEM results, suggesting the best adsorption capability among the other products.

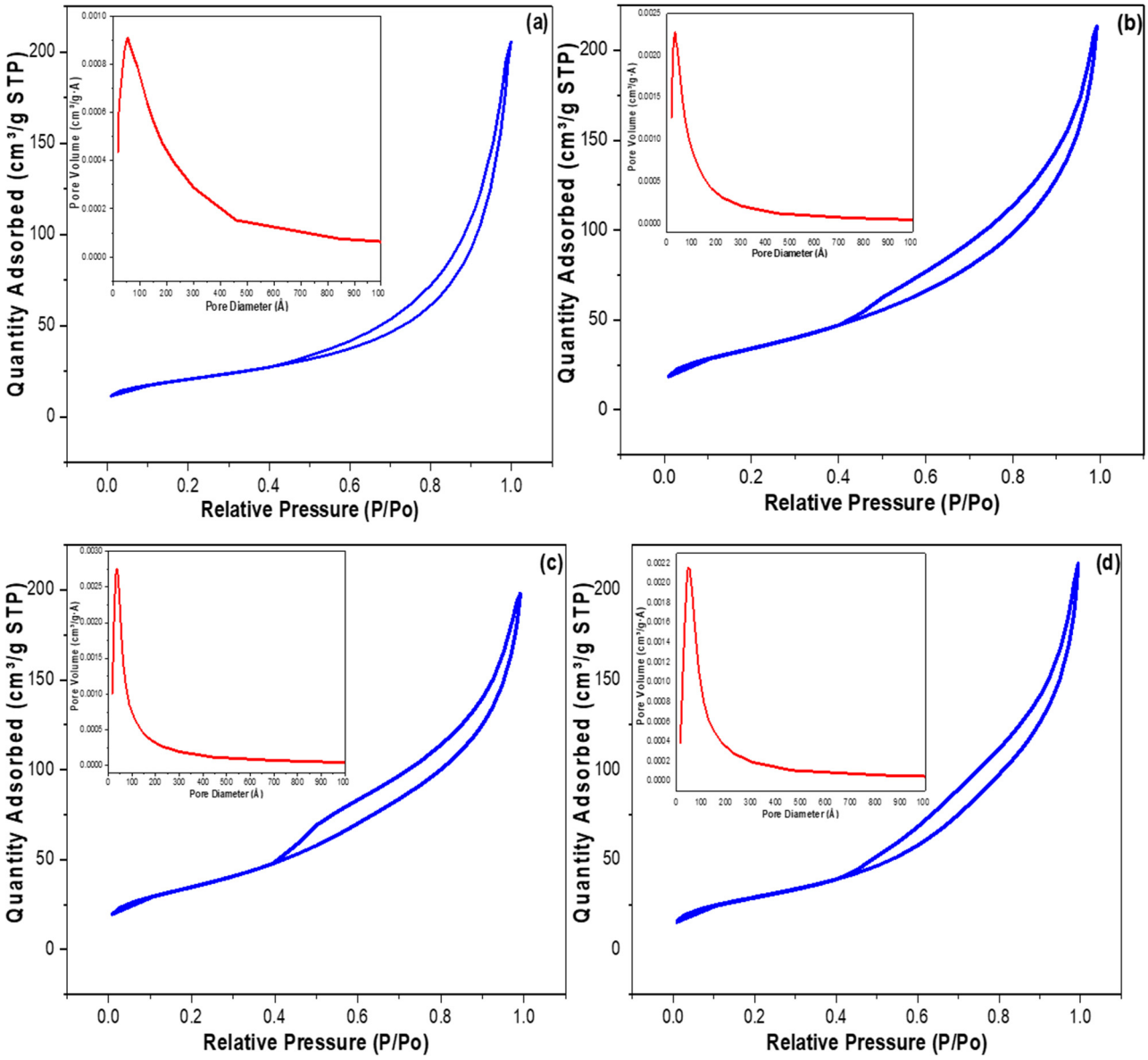

Figure 6. The nitrogen adsorption isotherms and pore size distribution results for (**a**) Al_2O_3 nanoparticle, (**b**) Al_2O_3-CuO, (**c**) Al_2O_3-NiO, and (**d**) Al_2O_3-CoO nanocomposites.

Table 1. The surface characteristics of the prepared Al_2O_3, Al_2O_3-CuO, Al_2O_3-NiO, and Al_2O_3-CoO nanomaterials.

Parameter	Al_2O_3	Al_2O_3-CuO	Al_2O_3-NiO	Al_2O_3-CoO
BET Surface Area (m^2 g^{-1})	74.709	123.984	125.636	105.653
average pore diameter (Å)	75.301	95.088	137.949	84.152
average pore volume (cm^3 g^{-1})	0.310	0.331	0.335	0.319

2.2. Adsorption of IGC

The contact-time impact on IGC adsorption on Al_2O_3, Al_2O_3-CuO, Al_2O_3-NiO, and Al_2O_3-CoO were presented in Figure 7a. Although the adsorption equilibrium was not reached for all sorbents until three hours, almost 90% of the total uptakes were taken within the first 60 min. The obtained qt values for Al_2O_3, Al_2O_3-CuO, Al_2O_3-NiO, and Al_2O_3-CoO were 57.2, 184.9, 198.8, and 149.1 mg $g^{-1,}$ respectively. These findings aligned with the high surface area revealed by the BET analysis for Al_2O_3-NiO nanocomposite, so it was selected for further investigations.

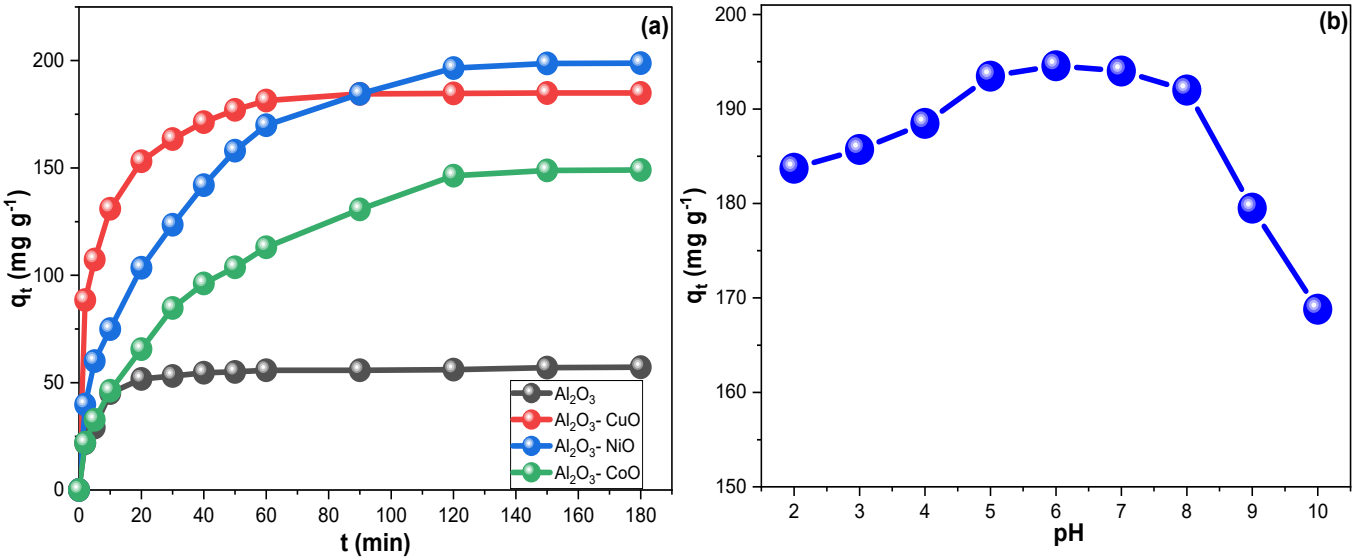

Figure 7. (**a**) The contact time study for IGC removal by the fabricated Al_2O_3, Al_2O_3-CuO, Al_2O_3-NiO, and Al_2O_3-CoO nanomaterials; (**b**) The pH influence on the removal of IGC dye by the Al_2O_3-NiO nanocomposite.

Figure 7b illustrates the pH impact on IGC removal by Al_2O_3-NiO nanocomposite. The IGC sorption decreased at low pHs but dropped more in high solution pHs. The performance of Al_2O_3-NiO nanocomposite was almost steady in the pH range of 5.0 to 8.0, with a preference of 6.0. This behavior can be explained in light of the IGC molecular structure since a high H^+ concentration may protonate the electron-rich sites on such ionic dye and cause repulsion between some spots of the metal oxide nanoparticles. In addition, the occupation of electron-rich sites on the IGC may decrease its availability and contribute to the sorption process. Conversely, the -OH groups may occupy some active-sorption sites on the sorbent in the high pH range [21,50,51].

2.3. Kinetics of IGC Adsorption

The adsorption order and rate-control mechanism for IGC adsorption on the Al_2O_3-NiO nanocomposite were investigated (Figure 8). The FOM and SOM for the IGC sorption possessed R^2 values of 0.970 and 0.934, respectively, with k_1 and k_2 values of 0.044 min^{-1} and 0.006 g mg^{-1} min^{-1}, respectively. Additionally, the rate-control mechanism examinations via the LDM and IM showed R^2 values of 0.997 and 0.985, respectively, and

exhibited equilibrium constants of 0.043 mg g^{-1} $min^{-0.5}$ and 15.486 min^{-1}, respectively. These findings illustrated that IGC sorption on the Al_2O_3-NiO followed the FOM, and the LDM controlled the sorption. [52,53]. Following the FOM and LDM mechanism was in line with the Al_2O_3-NiO particle being small and indicated a high affinity of IGC to the sorbent [54–56].

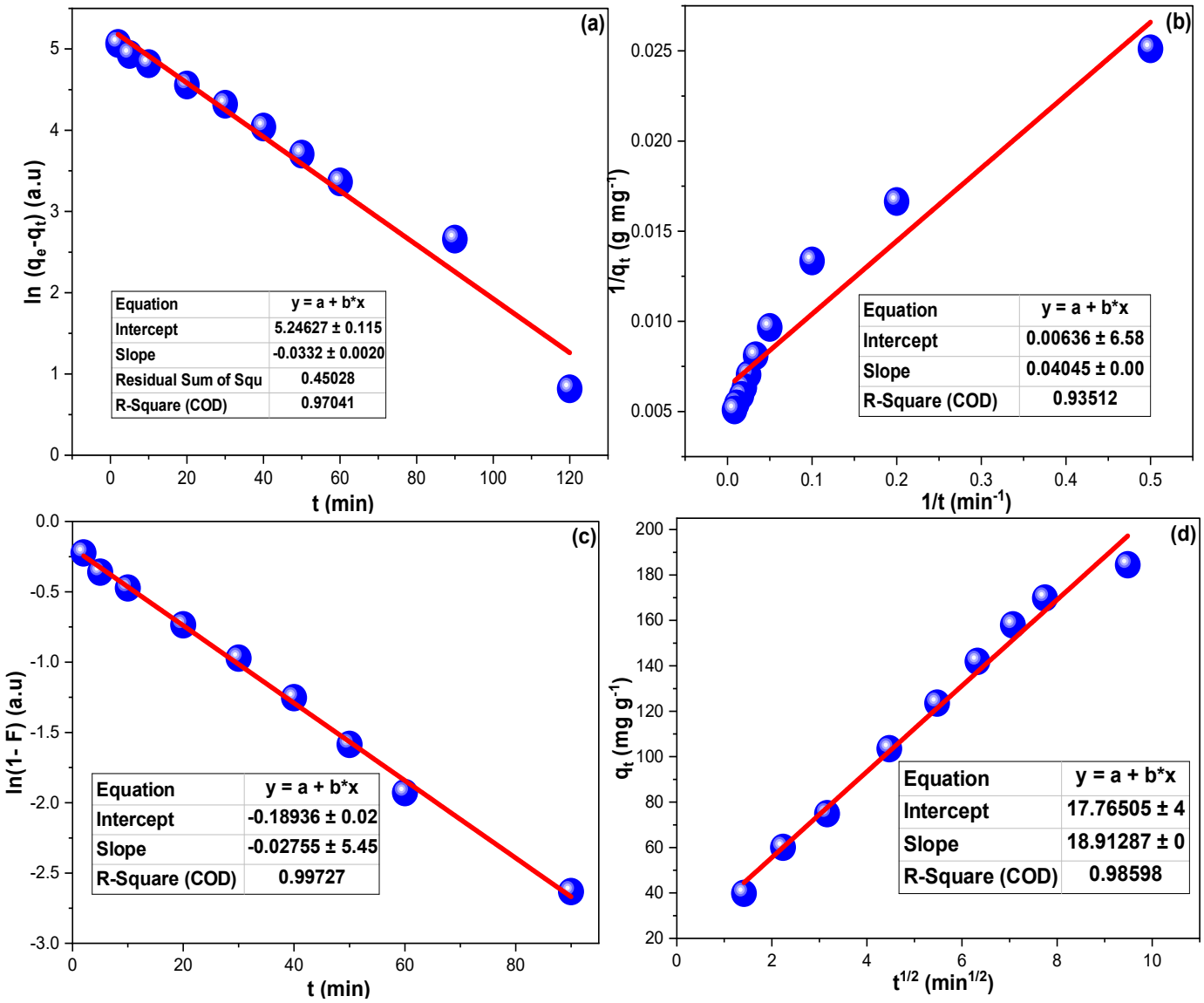

Figure 8. Kinetic investigations for the removal of IGC by the Al_2O_3-NiO nanocomposite, including (**a**) FOM, (**b**) SOM, (**c**) LDM, and (**d**) IM.

2.4. Adsorption Isotherms

The results obtained from the effect of concentrations were employed to investigate the adsorption isotherms. The monolayer and multilayer adsorption possibilities were studied via Langmuir (LIM) and Freundlich (FIM) isotherm models expressed in Equations (1) and (2), respectively.

$$\frac{1}{q_e} = \frac{1}{K_L\, q_m} \cdot \frac{1}{C_e} + \frac{1}{K_L} \tag{1}$$

$$\ln q_e = \ln K_F + \frac{1}{n} \ln C_e \tag{2}$$

where: K_L (L mg^{-1}) is the LIM constant; C_e (mg L^{-1}) is the equilibrium solution concentration; q_m (mg g^{-1}) is the computed maximum q_t; K_F (L mg^{-1}) and 1/n (arbitrary) are the equilibrium constant, and heterogeneity-factor of FIM, respectively. Figure 9 illustrates the LIM and FIM plots, and Table 2 presents their calculated results. The IGC adsorption on Al_2O_3-NiO fitted the LIM (R^2 = 0.943), while the FIM possessed an R^2 value of 0.910. Additionally, the Freundlich heterogeneity factor was 0.365, indicating favorable sorption for IGC on the Al_2O_3-NiO nanocomposite [57–61].

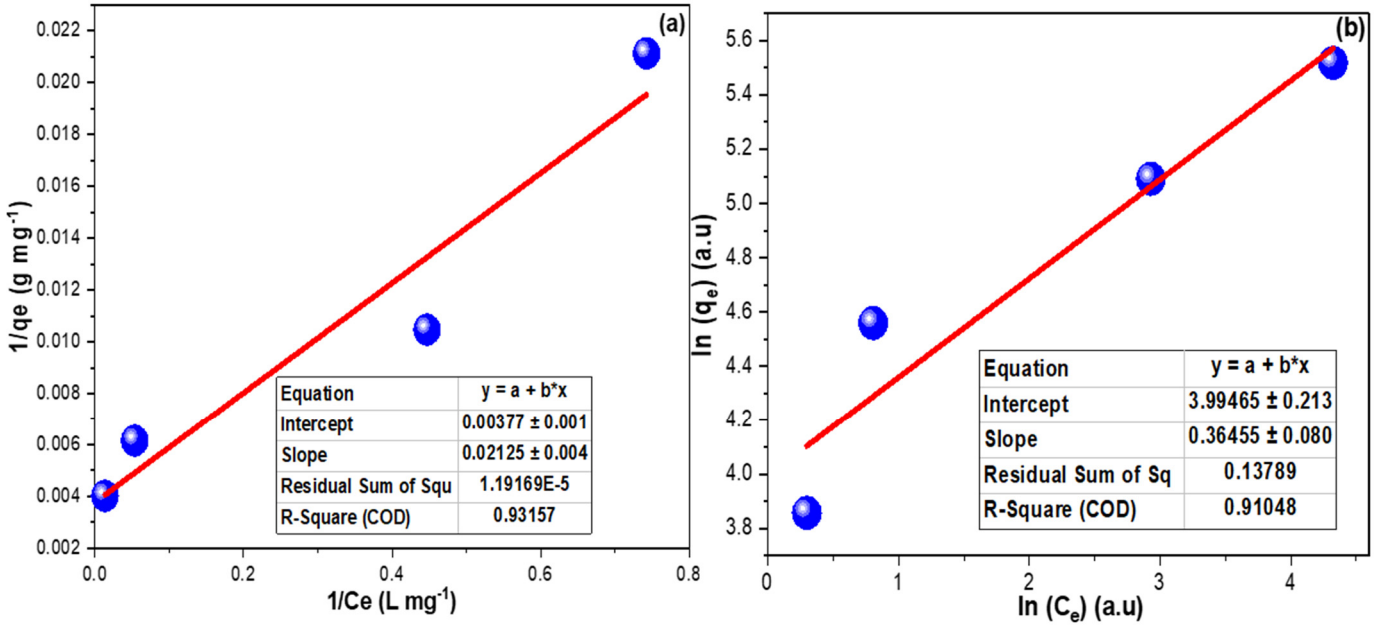

Figure 9. (**a**) LI and (**b**) FI investigations for the adsorption of IGC dye on the Al_2O_3-NiO nanocomposite at 20 °C from 25, 50, 100, and 200 mg L^{-1} IGC solutions.

Table 2. Isotherms and thermodynamic parameters for IGC adsorption onto the Al_2O_3-NiO nanocomposite.

Adsorption Isotherms					
Langmuir			Freundlich		
R^2 (a.u.)	K_L (L mg^{-1})	q_m (mg g^{-1})	R^2(a.u.)	K_f (L mg^{-1})	n^{-1} (a.u.)
0.932	265.024	0.178	0.910	54.307	0.365
Thermodynamic parameters					
Fed conc. (mg L^{-1})	ΔH° ($kJmol^{-1}$)	ΔS° ($kJmol^{-1}$)	ΔG° ($kJmol^{-1}$) 298 K	ΔG° ($kJmol^{-1}$) 308 K	ΔG° ($kJmol^{-1}$) 318 K
25	84.369	0.304	−6.372	−10.940	−15.507
50	55.616	0.211	−7.214	−10.377	−13.539
100	98.857	0.342	−2.919	−8.041	−13.164
200	66.112	0.225	−0.816	−4.184	−7.553

2.5. Thermodynamic

Figure 10a illustrates the temperature and concentration effects on IGC removal by Al_2O_3-NiO nanocomposite. Wourthmentioning, the Al_2O_3-NiO showed an experimental q_t of 456.3 mg g^{-1} from 200 mg L^{-1} at 50 °C. The direct proportionality between the obtained q_t values and the indicated temperature process is endothermic [62]. The thermodynamics were then explored for a better understanding of the IGC sorption on the Al_2O_3-NiO nanocomposite (Figure 8b). Equation (3) was utilized for computing the enthalpy (ΔH°)

and entropy (ΔS°), and their values were applied in Equation (4) to calculate the Gibbs-free-energy (ΔG°) and the results were in Table 2.

$$\ln K_c = \frac{\Delta H^\circ}{RT} + \frac{\Delta S^\circ}{R} \quad (3)$$

$$\Delta G^\circ = \Delta H^\circ - T\Delta S^\circ \quad (4)$$

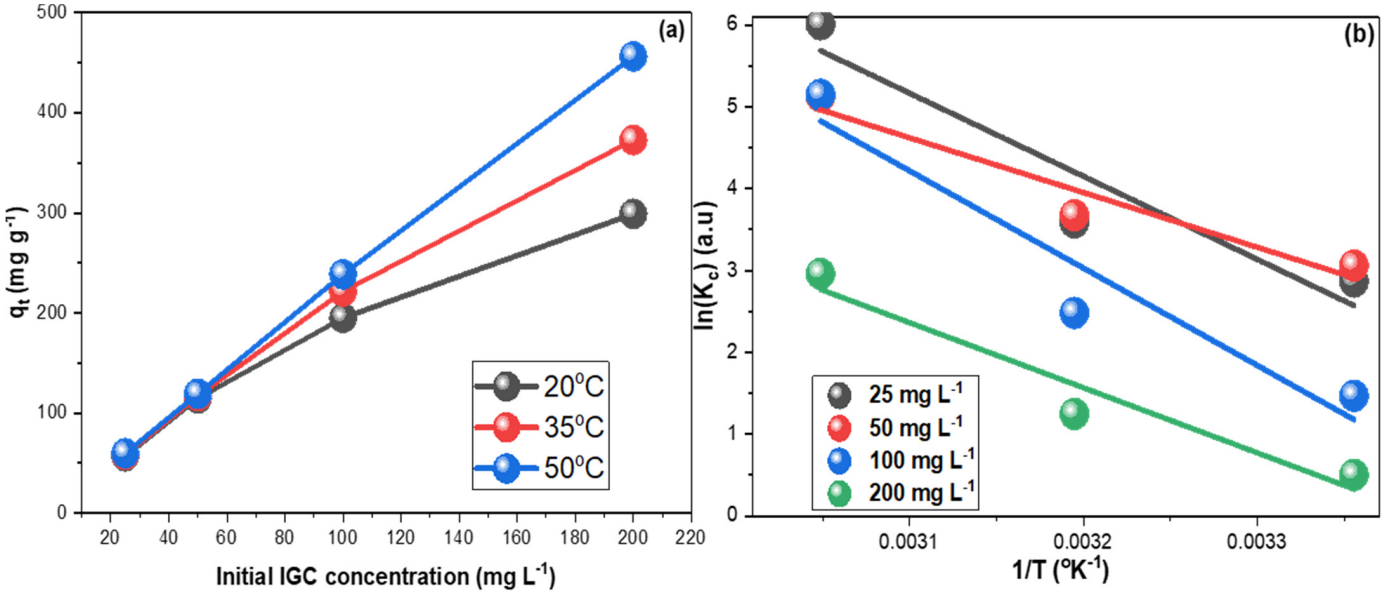

Figure 10. (**a**) The effect of IGC initial fed concentration on its sorption by the Al_2O_3-NiO nanocomposite at 20, 35, and 50 °C; (**b**) the thermodynamic investigation of IGC sorption by Al_2O_3-NiO nanocomposite from 25, 50, 100, and 200 mg L^{-1} solutions at 20, 35, and 50 °C.

As in all calculations, the value of 0.0081345 kJ mol^{-1} was applied as deal-gas-constant (R). The positive ΔH° values supported the previous endothermic suggestion. Moreover, the negative ΔG° values indicate the spontaneity of IGC sorption on the Al_2O_3-NiO nanocomposite [30]. Furthermore, having all the G° values less than 20 kJ mol^{-1} suggested a physisorption process [29]. The increased sorption spontineoutey as the concentration decreased implied the effectiveness of using this sorbent for water treatment, where low concentrations were expected.

2.6. Application to Natural Water Samples and Regeneration of Al_2O_3-NiO Nanocomposite

Figure 11a shows the results of using Al_2O_3-NiO nanocomposite for removing IGC from synthetically contaminated SW and GW. The nanocomposite possessed an average efficiency of 99.2% in treating the 5 and 10 mg L^{-1} IGC concentrations in each SW and GW sample. It is worth mentioning that the SW and GW polluted by 5.0 mg L^{-1} IGC concentrations were fully remediated. The lowest removal efficiency of 97.6 was attained with SW, which can be attributed to its high ion content.

Additionally, the reusability of the Al_2O_3-NiO nanocomposite was investigated (Figure 11b). The used Al_2O_3-NiO were filtered and sonicated with 10 mL ethanol for 10 min, 20 mL distilled water (DW), filtered, washed with distilled water, and dried at 105 °C for 2.0 h. The first removal efficiency was considered 100%, and the subsequent performances were determined relatively [63]. The Al_2O_3-NiO nanocomposite showed 93.6% average efficiency, with a 5.5% RSD value, and its lowest efficiency was 87.5%. This finding was in line with the sorptions fitting the LFDM, which indicated the ease of pollutant penetration into the inner sorbent sites and hindered recovery.

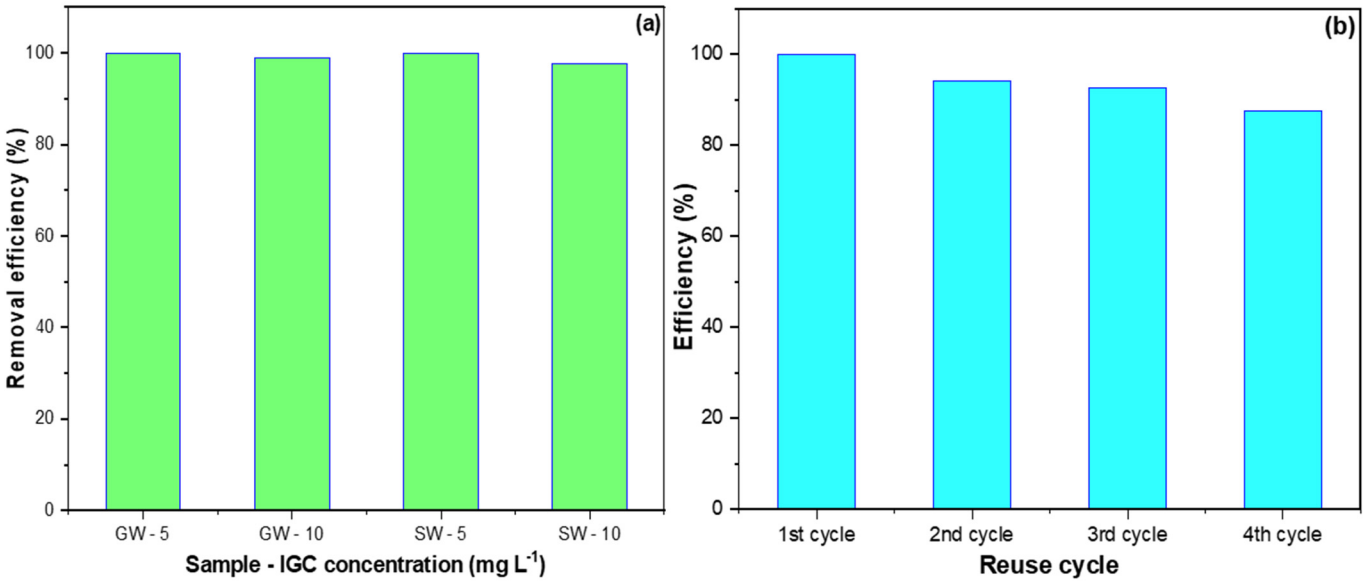

Figure 11. (**a**) Remediation of contaminated GW and SW using the Al_2O_3-NiO nanocomposite; (**b**) the reuse study of the Al_2O_3-NiO nanocomposite for removing IGC water.

3. Experimental

3.1. Materials

Aluminum trichloride hexahydrate ($AlCl_3.6H_2O$, 99%), and copper nitrate tetrahydrate ($Cu(NO_3)_2.3H_2O$, 98%), were purchased from LOBA CHEMIE (Mumbai, India). Cobalt acetate (II) ($Co(AC)_2$, 99%) was brought from Winlab (USA), and nickel nitrate ($Ni(NO_3)_2.6H_2O$, 98%) was obtained from BDH laboratory reagents (England). D(+) Glucose monohydrate (GL) was purchased from Riedel-de Haen (Germany). Indigo carmine was purchased from Fluka (Germany).

3.2. Synthesis of Al_2O_3 Nanoparticle and Its Composites

For the pure Al_2O_3 nanoparticles, 22.41 g of $AlCl_3$ were dissolved in 100 mL of distilled water. The solution was stirred with 10 g of glucose as a capping agent, and the mixture was heated to dryness. The formed solid was powdered, transferred into a porcelain dish, and calcined at 600 °C for 3.0 h. The Al_2O_3-CuO, Al_2O_3-NiO, and Al_2O_3-CoO nanocomposites were prepared in the same manner with the appropriate amount of ion salt to produce the Al_2O_3: metal-oxide composite of a 9:1 ratio.

3.3. Characterization of Al_2O_3 Nanoparticle and Its Composites

The surface morphology of the prepared nanomaterials was analyzed via scanning electron-energy-dispersive X-ray spectroscopy (FE-SEM-EDX, JSM-IT500HR). The bonding and functional groups were surveyed by FTIR spectrophotometer (Bruker TENSOR—USA). The surface characteristics were tested using a Micromeritics surface analyzer (ASAP 2020, USA). In addition, purity and crystallinity were examined using a powder X-ray diffractometer (Bruker, D8-Advance; Billerica, MA, USA).

3.4. Adsorption of IGC on Prepared Nanomaterials

The batch-experiment technique was used to investigate the activities of the Al_2O_3, Al_2O_3-CuO, Al_2O_3-NiO, and Al_2O_3-CoO in removing IGC from water. The contact time effect and kinetic investigations were performed by stirring 120 mL of the IGC solution (100 mg L^{-1}) with 50 mg of the sorbent. A 5.0 mL portion of each mixture was picked and filtered, and the IGC absorbance was measured by a UV-Vis-spectrophotometer (2600i, Shimadzu, Japan). The adsorption capacity (q_t, mg g^{-1}) at each time interval was computed by Equation (5), and accordingly, the best sorbent was selected for further investigation.

Additionally, the obtained results were employed to investigate the IGC's adsorption kinetics. Pseudo-first-order and pseudo-second-order kinetic models (FOM and SOM; Equations (6) and (7)) were utilized to examine the sorption rate. In addition, to figure out the step controlling the adsorption, the intra-particle, and liquid-film diffusion models (IM and LM; Equations (8) and (9)).

$$q_t = \frac{(C_o - C_t)\,V}{M} \tag{5}$$

$$\ln(q_e - q_t) = \ln(q_e) - k_1 \times t \tag{6}$$

$$\frac{1}{q_t} = \frac{1}{k_2 q_e^2\, t} + \frac{1}{q_e} \tag{7}$$

$$q_t = K_{IM} \times t^{\frac{1}{2}} + C_i \tag{8}$$

$$\ln(1 - F) = -K_{LM} * t \tag{9}$$

where: C_o, C_t (mg L^{-1}) resents the dye concentrations at time zero and t; V (L) and M (g) present the volume of dye solution and mass of sorbent, respectively; k_1(min^{-1}): the FOM rate constant; k_2 (g mg^{-1} min^{-1}): rate-constant of the SOM; K_{IM} (mg g^{-1} $min^{-0.5}$) and K_{LM} (min^{-1}): the IM and LDM constants; the q_e (mg g^{-1}) is the equilibrium adsorption capacity; C_i (mg g^{-1}): the boundary-layer-thickness parameter.

Furthermore, the adsorption of IGC on the sorbent was tested under serial solution pH. The 100 mg L^{-1} IGC solution was adjusted to a pH value from 2.0 to 10.0. 100 mL of the adjusted solution was stirred with 50 mg sorbent to the equilibrium time, and the rest of the solution was used as the standard.

3.5. Adsorption Equilibria

The initial IGC concentration impact on its removal by the best sorbent was tested utilizing 25, 50, 75, and 100 mg L^{-1} IGC concentrations. Additionally, to study the effect of temperature on IGC removal, sorption from the previously mentioned concentrations was performed at 20, 35, and 50 °C. The obtained results were utilized to investigate the sorption isotherms and thermodynamics.

3.6. Application to Natural Water Samples

A groundwater sample (GW) was picked from Sudhir city (≈165 km from Riyadh-KSA), and the Seawater (SW) was collected from Aldhran coast-KSA. Each water sample was spiked with the appropriate amount of IGC solution (100 mg L^{-1}) to obtain 5.0 and 10.0 mg L^{-1} concentrations. The contaminated GW and SW were stirred with 50 mg of sorbent, and the removal efficiency was calculated using Equation (10).

$$\%E = \frac{(C_o - C_t) \times 100}{C_o} \tag{10}$$

4. Conclusions

Al_2O_3, Al_2O_3-CuO, Al_2O_3-NiO, and Al_2O_3-CoO were prepared via a simple and fast route using glucose as the capping material. The influence on the characteristics of the prepared nanomaterials was kept to the ion type by uniforming the synthesis conditions. The particle sizes of the synthesized Al_2O_3, Al_2O_3-CuO, Al_2O_3-NiO, and Al_2O_3-CoO were less than 25 nm. The Al_2O_3-NiO showed the smallest particle size (11 to 14 nm) and the highest surface area. All sorbents were tested for removing IGC from water, and Al_2O_3-NiO possessed the best q_t value among the other sorbents, so it was selected for further studies. The IGC adsorption on the Al_2O_3-NiO nanocomposite fitted the FOM, and the LFM influenced IGC removal. The equilibrium investigations revealed the agreement of IGC adsorption on the Al_2O_3-NiO nanocomposite to the LI model. The thermodynamic results indicated an endothermic, spontaneous, and physisorption nature. The Al_2O_3-NiO

nanocomposite remediated SW and GW spiked with a 5.0 mg L^{-1} IGC concentration. The reuse study showed 93.3% average efficiency during four successive cycles. This study indicated that doping Al_2O_3 by NiO produced a better sorbent than Al_2O_3, Al_2O_3-CuO, and Al_2O_3-CoO.

Funding: This research received no external funding.

Data Availability Statement: The data of this manuscript is available under reasonable request.

Conflicts of Interest: The authors declare that they have no known competing financial interest or personal relationships that could have influenced the work reported in this paper.

References

1. Elamin, M.R.; Ibnaouf, K.H.; Elamin, N.Y.; Adam, F.A.; Alolayan, A.H.; Abdulkhair, B.Y. Spontaneous Adsorption and Efficient Photodegradation of Indigo Carmine under Visible Light by Bismuth Oxyiodide Nanoparticles Fabricated Entirely at Room Temperature. *Inorganics* **2022**, *10*, 65. [CrossRef]
2. Rahbar-Shamskar, K.; Azar, P.A.; Rashidi, A.; Baniyaghoob, S.; Yousefi, M. Synthesis of micro/mesoporous carbon adsorbents by in-situ fast pyrolysis of reed for recovering gasoline vapor. *J. Clean. Prod.* **2020**, *259*, 120832. [CrossRef]
3. Silva, A.R.; Cavaleiro, A.J.; Soares, O.S.G.; Braga, C.S.; Salvador, A.F.; Pereira, M.F.R.; Alves, M.M.; Pereira, L. Detoxification of ciprofloxacin in an anaerobic bioprocess supplemented with magnetic carbon nanotubes: Contribution of adsorption and biodegradation mechanisms. *Int. J. Mol. Sci.* **2021**, *22*, 2932. [CrossRef] [PubMed]
4. Bożęcka, A.; Orlof-Naturalna, M.; Kopeć, M. Methods of Dyes Removal from Aqueous Environment. *J. Ecol. Eng.* **2021**, *22*, 111–118. [CrossRef]
5. Ho, S.; Protection, E. Removal of Dyes from Wastewater by Adsorption onto Activated Carbon: Mini Review. *J. Geosci. Environ. Prot.* **2020**, *8*, 120. [CrossRef]
6. Sivaprakash, S.; Kumar, P.S.; Krishna, S. Adsorption study of various dyes on Activated Carbon Fe_3O_4 Magnetic Nano Composite. *Int. J. Appl. Chem.* **2017**, *13*, 255–266.
7. Dastgerdi, Z.H.; Meshkat, S.S.; Esrafili, M.D. Enhanced adsorptive removal of Indigo carmine dye performance by functionalized carbon nanotubes based adsorbents from aqueous solution: Equilibrium, kinetic, and DFT study. *J. Nanostruct. Chem.* **2019**, *9*, 323–334. [CrossRef]
8. Forgacs, E.; Cserháti, T.; Oros, G. Removal of synthetic dyes from wastewaters: A review. *Environ. Int.* **2004**, *30*, 953–971. [CrossRef]
9. Labiadh, L.; Barbucci, A.; Carpanese, M.P.; Gadri, A.; Ammar, S.; Panizza, M. Direct and indirect electrochemical oxidation of Indigo Carmine using PbO_2 and $TiRuSnO_2$. *J. Solid State Electrochem.* **2017**, *21*, 2167–2175. [CrossRef]
10. Ullah, F.; Othman, M.B.H.; Javed, F.; Ahmad, Z.; Akil, H.M. Classification, processing and application of hydrogels: A review. *Mater. Sci. Eng. C* **2015**, *57*, 414–433. [CrossRef]
11. Gemeay, A.H.; Aboelfetoh, E.F.; El-Sharkawy, R.G. Immobilization of green synthesized silver nanoparticles onto amino-functionalized silica and their application for indigo carmine dye removal. *Water Air Soil Pollut.* **2018**, *229*, 16. [CrossRef]
12. Emik, S.; Işık, S.; Yıldırım, E. Simultaneous removal of cationic and anionic dyes from binary solutions using carboxymethyl chitosan based IPN Type resin. *J. Polym. Environ.* **2021**, *29*, 1963–1977. [CrossRef]
13. Zein, R.; Hevira, L.; Fauzia, S.; Ighalo, J.O. The improvement of indigo carmine dye adsorption by *Terminalia catappa* shell modified with broiler egg white. *Biomass Convers. Biorefin.* **2022**, 1–18. [CrossRef]
14. Topare, N.S.; Bokil, S.A. Adsorption of textile industry effluent in a fixed bed column using activated carbon prepared from agro-waste materials. *Mater. Today Proc.* **2021**, *43*, 530–534. [CrossRef]
15. Yurtsever, A.; Basaran, E.; Ucar, D.; Sahinkaya, E. Self-forming dynamic membrane bioreactor for textile industry wastewater treatment. *Sci. Total Environ.* **2021**, *751*, 141572. [CrossRef]
16. Feng, Q.; Gao, B.; Yue, Q.; Guo, K. Flocculation performance of papermaking sludge-based flocculants in different dye wastewater treatment: Comparison with commercial lignin and coagulants. *Chemosphere* **2021**, *262*, 128416. [CrossRef]
17. Othman, M.H.D.; Adam, M.R.; Kamaludin, R.; Ismail, N.J.; Rahman, M.A.; Jaafar, J. Advanced Membrane Technology for Textile Wastewater Treatment. In *Membrane Technology Enhancement for Environmental Protection and Sustainable Industrial Growth*; Springer: Cham, Switzerland, 2021; pp. 91–108.
18. Ahsan, M.A.; Fernandez-Delgado, O.; Deemer, E.; Wang, H.; El-Gendy, A.A.; Curry, M.L.; Noveron, J.C. Carbonization of Co-BDC MOF results in magnetic C@ Co nanoparticles that catalyze the reduction of methyl orange and 4-nitrophenol in water. *J. Mol. Liq.* **2019**, *290*, 111059. [CrossRef]
19. Ahsan, M.A.; Deemer, E.; Fernandez-Delgado, O.; Wang, H.; Curry, M.L.; El-Gendy, A.A.; Noveron, J.C. Fe nanoparticles encapsulated in MOF-derived carbon for the reduction of 4-nitrophenol and methyl orange in water. *Catal. Commun.* **2019**, *130*, 105753. [CrossRef]
20. Ahsan, M.A.; Jabbari, V.; El-Gendy, A.A.; Curry, M.L.; Noveron, J.C. Ultrafast catalytic reduction of environmental pollutants in water via MOF-derived magnetic Ni and Cu nanoparticles encapsulated in porous carbon. *Appl. Surf. Sci.* **2019**, *497*, 143608. [CrossRef]

21. Elamin, M.R.; Abdulkhair, B.Y.; Elzupir, A.O. Removal of ciprofloxacin and indigo carmine from water by carbon nanotubes fabricated from a low-cost precursor: Solution parameters and recyclability. *Ain Shams Eng. J.* **2022**, 101844. [CrossRef]
22. Chowdhury, M.F.; Khandaker, S.; Sarker, F.; Islam, A.; Rahman, M.T.; Awual, M.R. Current treatment technologies and mechanisms for removal of indigo carmine dyes from wastewater: A review. *J. Mol. Liq.* **2020**, *318*, 114061. [CrossRef]
23. Harrache, Z.; Abbas, M.; Aksil, T.; Trari, M. Thermodynamic and kinetics studies on adsorption of Indigo Carmine from aqueous solution by activated carbon. *Microchem. J.* **2019**, *144*, 180–189. [CrossRef]
24. Oberoi, A.S.; Jia, Y.; Zhang, H.; Khanal, S.K.; Lu, H. Insights into the fate and removal of antibiotics in engineered biological treatment systems: A critical review. *Environ. Sci. Technol.* **2019**, *53*, 7234–7264. [CrossRef] [PubMed]
25. Jones, O.A.; Lester, J.N.; Voulvoulis, N. Pharmaceuticals: A threat to drinking water? *Trends Biotechnol.* **2005**, *23*, 163–167. [CrossRef]
26. Hussin, F.; Aroua, M.K.; Kassim, M.A. Transforming Plastic Waste into Porous Carbon for Capturing Carbon Dioxide: A Review. *Energies* **2021**, *14*, 8421. [CrossRef]
27. Almufarij, R.S.; Abdulkhair, B.Y.; Salih, M.; Aldosari, H.; Aldayel, N.W. Optimization, Nature, and Mechanism Investigations for the Adsorption of Ciprofloxacin and Malachite Green onto Carbon Nanoparticles Derived from Low-Cost Precursor via a Green Route. *Molecules* **2022**, *27*, 4577. [CrossRef]
28. Ghoniem, M.G.; Ali, F.A.M.; Abdulkhair, B.Y.; Elamin, M.R.A.; Alqahtani, A.M.; Rahali, S.; Ben Aissa, M.A. Highly selective removal of cationic dyes from wastewater by MgO nanorods. *Nanomaterials* **2022**, *12*, 1023. [CrossRef]
29. Elamin, M.R.; Abdulkhair, B.Y.; Algethami, F.K.; Khezami, L. Linear and nonlinear investigations for the adsorption of paracetamol and metformin from water on acid-treated clay. *Sci. Rep.* **2021**, *11*, 13606. [CrossRef]
30. Elamin, M.R.; Abdulkhair, B.Y.; Elzupir, A.O. Insight to aspirin sorption behavior on carbon nanotubes from aqueous solution: Thermodynamics, kinetics, influence of functionalization and solution parameters. *Sci. Rep.* **2019**, *9*, 12795. [CrossRef]
31. Zhukovskii, Y.F.; Piskunov, S.; Lisovski, O.; Bocharov, D.; Evarestov, R.A. Doped 1D Nanostructures of Transition-metal Oxides: First-principles Evaluation of Photocatalytic Suitability. *Isr. J. Chem.* **2017**, *57*, 461–476. [CrossRef]
32. Prins, R. On the structure of γ-Al_2O_3. *J. Catal.* **2020**, *392*, 336–346. [CrossRef]
33. Gao, X.; Ge, Z.; Zhu, G.; Wang, Z.; Ashok, J.; Kawi, S. Anti-coking and anti-sintering Ni/Al_2O_3 catalysts in the dry reforming of methane: Recent progress and prospects. *Catalysts* **2021**, *11*, 1003. [CrossRef]
34. Cui, K.; Zhang, Y.; Fu, T.; Hussain, S.; Saad Algarni, T.; Wang, J.; Zhang, X.; Ali, S. Effects of Cr_2O_3 content on microstructure and mechanical properties of Al_2O_3 matrix composites. *Coatings* **2021**, *11*, 234. [CrossRef]
35. Khan, M.; Janjua, N.K.; Khan, S.; Qazi, I.; Ali, S.; Saad Algarni, T. Electro-oxidation of ammonia at novel Ag_2O-PrO_2/γ-Al_2O_3 catalysts. *Coatings* **2021**, *11*, 257. [CrossRef]
36. Khan, S.; Shah, S.S.; Anjum, M.A.R.; Khan, M.R.; Janjua, N.K. Electro-oxidation of ammonia over copper oxide impregnated γ-Al_2O_3 nanocatalysts. *Coatings* **2021**, *11*, 313. [CrossRef]
37. Yeşiltepe Özcelik, D.; Ebin, B.; Stopic, S.; Gürmen, S.; Friedrich, B. Mixed oxides NiO/ZnO/Al_2O_3 synthesized in a single step via ultrasonic spray pyrolysis (USP) method. *Metals* **2022**, *12*, 73. [CrossRef]
38. Elsayed, A.M.; Rabia, M.; Shaban, M.; Aly, A.H.; Ahmed, A.M. Preparation of hexagonal nanoporous Al_2O_3/TiO_2/TiN as a novel photodetector with high efficiency. *Sci. Rep.* **2021**, *11*, 17572. [CrossRef] [PubMed]
39. Kobayashi, Y.; Horiguchi, J.; Kobayashi, S.; Yamazaki, Y.; Omata, K.; Nagao, D.; Konno, M.; Yamada, M. Effect of NiO content in mesoporous NiO–Al_2O_3 catalysts for high pressure partial oxidation of methane to syngas. *Appl. Catal. A Gen.* **2011**, *395*, 129–137. [CrossRef]
40. Liu, H.; Ning, G.; Gan, Z.; Lin, Y. A simple procedure to prepare spherical α-alumina powders. *Mater. Res. Bull.* **2009**, *44*, 785–788. [CrossRef]
41. Di, S.; Gong, L.; Zhou, B. Physics. Precipitated synthesis of Al_2O_3-ZnO nanorod for high-performance symmetrical supercapacitors. *Mater. Chem. Phys.* **2020**, *253*, 123289. [CrossRef]
42. Padil, V.V.T.; Černík, M. Green synthesis of copper oxide nanoparticles using gum karaya as a biotemplate and their antibacterial application. *Int. J. Nanomed.* **2013**, *8*, 889.
43. Rajeswari, V.D.; Khalifa, A.S.; Elfasakhany, A.; Badruddin, I.A.; Kamangar, S.; Brindhadevi, K.J.A.N. Green and ecofriendly synthesis of cobalt oxide nanoparticles using *Phoenix dactylifera* L: Antimicrobial and photocatalytic activity. *Appl. Nanosci.* **2021**, 1–9. [CrossRef]
44. Dharmaraj, N.; Prabu, P.; Nagarajan, S.; Kim, C.; Park, J.; Kim, H.Y. Synthesis of nickel oxide nanoparticles using nickel acetate and poly (vinyl acetate) precursor. *Mater. Sci. Eng. B* **2006**, *128*, 111–114. [CrossRef]
45. Afkhami, A.; Saber-Tehrani, M.; Bagheri, H. Simultaneous removal of heavy-metal ions in wastewater samples using nano-alumina modified with 2, 4-dinitrophenylhydrazine. *J. Hazard. Mater.* **2010**, *181*, 836–844. [CrossRef] [PubMed]
46. Prabhakar, R.; Samadder, S.R. Low cost and easy synthesis of aluminium oxide nanoparticles for arsenite removal from groundwater: A complete batch study. *J. Mol. Liq.* **2018**, *250*, 192–201. [CrossRef]
47. Nallusamy, S.; Sujatha, K. Experimental analysis of nanoparticles with cobalt oxide synthesized by coprecipitation method on electrochemical biosensor using FTIR and TEM. *Mater. Today Proc.* **2021**, *37*, 728–732. [CrossRef]
48. Sun, S.; Liang, F.; Tang, L.; Wu, J.; Ma, C. Exploitation. Microstructural investigation of gas shale in Longmaxi formation, Lower Silurian, NE Sichuan basin, China. *Energy Explor. Exploit.* **2017**, *35*, 406–429. [CrossRef]

49. Thommes, M.; Kaneko, K.; Neimark, A.V.; Olivier, J.P.; Rodriguez-Reinoso, F.; Rouquerol, J.; Sing, K.S.W. Physisorption of gases, with special reference to the evaluation of surface area and pore size distribution (IUPAC Technical Report). *Pure Appl. Chem.* **2015**, *87*, 1051–1069. [CrossRef]
50. Zhang, J.-Z.; Huang, X.-L. Effect of temperature and salinity on phosphate sorption on marine sediments. *Environ. Sci. Technol.* **2011**, *45*, 6831–6837. [CrossRef]
51. Flower, H.; Rains, M.; Lewis, D.; Zhang, J.-Z.; Price, R. Saltwater intrusion as potential driver of phosphorus release from limestone bedrock in a coastal aquifer. *Estuar. Coast. Shelf Sci.* **2017**, *184*, 166–176. [CrossRef]
52. Kyzas, G.Z.; Deliyanni, E.A. Modified activated carbons from potato peels as green environmental-friendly adsorbents for the treatment of pharmaceutical effluents. *Chem. Eng. Res. Des.* **2015**, *97*, 135–144. [CrossRef]
53. An, B.J.P. Cu (II) and As (V) adsorption kinetic characteristic of the multifunctional amino groups in chitosan. *Processes* **2020**, *8*, 1194. [CrossRef]
54. Hameed, B.; El-Khaiary, M.I. Malachite green adsorption by rattan sawdust: Isotherm, kinetic and mechanism modeling. *J. Hazard. Mater.* **2008**, *159*, 574–579. [CrossRef] [PubMed]
55. Vadivelan, V.; Kumar, K.V. Equilibrium, kinetics, mechanism, and process design for the sorption of methylene blue onto rice husk. *J. Colloid Interface Sci.* **2005**, *286*, 90–100. [CrossRef]
56. Mohan, D.; Singh, K.P. Single-and multi-component adsorption of cadmium and zinc using activated carbon derived from bagasse—An agricultural waste. *Water Res.* **2002**, *36*, 2304–2318. [CrossRef]
57. Hamdaoui, O.; Naffrechoux, E. Modeling of adsorption isotherms of phenol and chlorophenols onto granular activated carbon: Part I. Two-parameter models and equations allowing determination of thermodynamic parameters. *J. Hazard. Mater.* **2007**, *147*, 381–394. [CrossRef]
58. Kumar, P.S.; Ramalingam, S.; Senthamarai, C.; Niranjanaa, M.; Vijayalakshmi, P.; Sivanesan, S. Adsorption of dye from aqueous solution by cashew nut shell: Studies on equilibrium isotherm, kinetics and thermodynamics of interactions. *Desalination* **2010**, *261*, 52–60. [CrossRef]
59. Aljeboree, A.M.; Alshirifi, A.N.; Alkaim, A.F. Kinetics and equilibrium study for the adsorption of textile dyes on coconut shell activated carbon. *Arab. J. Chem.* **2017**, *10*, S3381–S3393. [CrossRef]
60. Jain, S.N.; Shaikh, Z.; Mane, V.S.; Vishnoi, S.; Mawal, V.N.; Patel, O.R.; Bhandari, P.S.; Gaikwad, M.S. Nonlinear regression approach for acid dye remediation using activated adsorbent: Kinetic, isotherm, thermodynamic and reusability studies. *Microchem. J.* **2019**, *148*, 605–615. [CrossRef]
61. Do, D.D. *Adsorption Analysis: Equilibria and Kinetics*; Imperial College Press: London, UK, 1998; Volume 2.
62. Darryle, C.M.; Acayanka, E.; Takam, B.; Line, L.N.; Kamgang, G.Y.; Laminsi, S.; Sellaoui, L.; Bonilla-Petriciolet, A. Influence of plasma-based surface functionalization of palm fibers on the adsorption of diclofenac from water: Experiments, thermodynamics and removal mechanism. *J. Water Process Eng.* **2021**, *43*, 102254. [CrossRef]
63. Wang, N.; Han, Y.; Li, S. Adsorption characteristic of Cr (VI) onto different activated coal fly ashes: Kinetics, thermodynamic, application feasibility, and error analysis. *Water Air Soil Pollut.* **2019**, *230*, 1–13. [CrossRef]